RESEARCH ARTICLE

Key Points:
- Stacking autocorrelations of *P* coda wave forms reveal *P* and *S* wave reflectivity
- Spectral whitening normalization enriches high-frequency content and thus allows access to shallow ice-rock interface
- Estimates on thickness and *P* over *S* wave speed ratio of the Antarctic ice sheet confirm previous results

Supporting Information:
- Supporting Information S1

Correspondence to:
T.-S. Phạm,
thanhson.pham@anu.edu.au

Antarctic Ice Properties Revealed From Teleseismic *P* Wave Coda Autocorrelation

Thanh-Son Phạm[1] ID **and Hrvoje Tkalčić[1]** ID

[1]Research School of Earth Sciences, The Australian National University, Canberra, ACT, Australia

Abstract Antarctica is largely covered by an ice cap of a variable thickness characterized by relatively low density and seismic velocities. Passive seismological deployments have a limited use in imaging a thin ice layer because of the dominance of a relatively low-frequency content in the teleseismic wavefield. Here we use passive seismological data and an improved autocorrelation method utilizing *P* wave coda to image the ice cover. The resulting autocorrelograms are interpreted as reflectivity records from a virtual source on the surface and reflection pulses at the ice base. We convert the reflection delay of *P* waves to the ice thickness measurements using a homogeneous *P* wave speed compatible with previous studies. Apart from *P* wave reflectivity, we obtain *S* wave reflectivity from the autocorrelation of radial component. The ratio of *S* wave and *P* wave reflection times represents a measurement of the *P* over *S* wave speed ratio (and Poisson's ratio). The successful application to unveil the Antarctic ice sheet properties presented here opens a way for future studies to measure properties of the ice cover in Antarctica, other continents, and icy planets in future space missions.

1. Introduction

In a horizontally stratified media, the autocorrelation of seismic records of near-vertically arriving plane waves can be deployed to retrieve the structural reflection response beneath a seismic station (Claerbout, 1968; Frasier, 1970). This principle is appealing because it utilizes seismic data of just one recording component (e.g., vertical or radial). Thus, the autocorrelation analysis can be used to reprocess old data archives of which only one, for example, only vertical, component is available (Kennett et al., 2015) or in planetary seismology where each recording component is invaluable due to the high cost of deploying a seismometer in space missions (e.g., Nishitsuji et al., 2016; Zhan et al., 2014). Three-component data enable the extraction of reflection responses from each component independently, which provides additional constraints on elastic structures beneath a station.

In this study, we apply an improved autocorrelation method (Phạm & Tkalčić, 2017) that uses a part of earthquake seismograms following the *P* wave arrivals, namely, the *P* wave coda (e.g., Paulssen et al., 1993), to image the ice sheet covering the Antarctic continent. Although several authors have been utilizing the autocorrelation principle to a large volume of continuous ambient noise records to extract near-vertical reflections from subsurface discontinuities (Becker & Knapmeyer-Endrun, 2018; Gorbatov et al., 2013; Kennett et al., 2015; Oren & Nowack, 2017; Saygin et al., 2017), the approach relying on earthquakes introduces two main advantages. First, because the incidence of *P* waves arriving from distance earthquakes is near vertical, it facilitates the extraction of desired vertical reflectivity (Ruigrok & Wapenaar, 2012; Sun & Kennett, 2016). Consequently, the coda processing requires significantly smaller data volume as well as computational resources. Second, body waves from teleseismic earthquakes, for example, *P* or *S* waves, generally have richer content in high-frequency band than ambient noise data; thus, they enable the higher resolution of relatively shallow seismic discontinuities. Note that the use of teleseismic *P* wave arrivals is similar to the use of core-sensitive phases, for example, PKIKP in the method termed "global-phase seismic interferometry" by Ruigrok and Wapenaar (2012), although here we employ a markedly different data-processing procedure.

Antarctica is largely covered by a thick permanent glacier of ~2,000 m thickness on average and up to ~5,000 m thickness (Fretwell et al., 2013), while bedrock outcrops are limited to the coastal skirts or mountainous provinces of the continent. Because the Antarctic ice sheet plays a vital role in the ecosystem as the largest freshwater reservoir on Earth, direct ice thickness measurements have been conducted for several decades (Lythe et al., 2001). A popular method, radio-echo sounding, employs very high frequency electromagnetic waves that are transparent to cold ice and mainly get reflected (echoed) at the ice
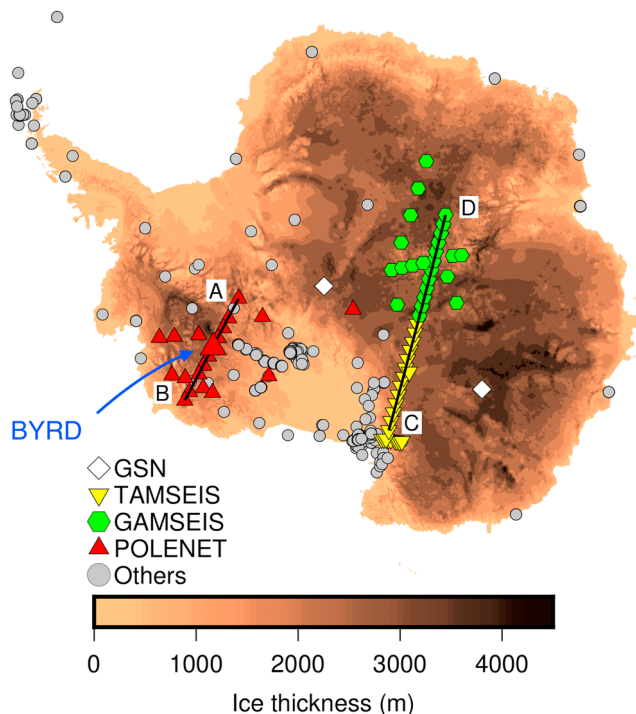
Figure 1. Map of Antarctica featuring data from BEDMAP2 ice thickness database (Fretwell et al., 2013). All seismic stations are accessed through the IRIS Data Center. Individual elements of network TAMSEIS (Lawrence et al., 2006) are marked with yellow inverted triangles, those of GAMSEIS (Lloyd et al., 2013) are marked with green hexagons, and those of POLENET (Chaput et al., 2014) are marked with red triangles. Two stations, QSPA (South Pole) and CCD (Concordia base) are permanently installed over ice (white diamonds). Autocorrelation results of the pilot station, BYRD, are shown in Figures 2 and 4. Lines AB and CD show seismic profiles featured in Figure 7. Stations denoted with gray circles are not used in this study because either they are deployed on bedrock or their data are not publically available.

surface, the ice base, and other internal discontinuities (Bingham & Siegert, 2007; Plewes & Hubbard, 2001). The ice thickness can then be calculated from the delay time between echoes and nearly constant electromagnetic wave speed in ice. The method provides a large database of high-quality measurements for the ice thickness. The measurements alongside minor contributions from other methods, such as seismic profiling and drilling, are interpolated into regularly gridded data sets of the ice thickness over the entire continent to produce comprehensive maps, that is, BEDMAP (Lythe et al., 2001) and BEDMAP2 (Fretwell et al., 2013).

Because of the ever-growing seismograph networks deployed over ice in Antarctica for cryoseismic studies (Podolskiy & Walter, 2016), several passive seismological methods widely used to study the crustal structures elsewhere have also been deployed to estimate the ice thickness complementary to the active-source measurements. Those methods provide local measurements to the recording sites with less logistical support (Yan et al., 2018). For example, pioneering studies have demonstrated the successful applications of the receiver function as well as the horizontal versus vertical spectral ratio methods. Particularly, Hansen et al. (2010) used the P wave receiver function technique (Langston, 1979) that relies on P to S wave energy conversion at subsurface interfaces, to estimate ice thickness under a number of over-ice stations in the Gamburtsev Mountains. This technique was also used to constrain an internal layer (Wittlinger & Farra, 2012, 2015) or a sedimentary layer sandwiched between ice and crustal bedrock (Anandakrishnan & Winberry, 2004; Chaput et al., 2014). The second class of methods use the spectral ratio between vertical and horizontal wave forms to reveal resonance peaks of P or S waves reverberated within a thin layer of snow (e.g., Lévêque et al., 2010) or ice (e.g., Diez et al., 2016) or a water layer beneath an ice shelf (Zhan et al., 2014). Most recently, Yan et al. (2018) presented a successful application of the horizontal-to-vertical (H/V) spectral ratio method to estimate the ice thickness beneath a large number of seismic stations distributed over Antarctica. Because the method needed a relatively short record of ambient noise of few days, this approach can be potentially used in future temporary deployments.

However, both passive seismological methods mentioned above require all three component recorders (one vertical and two horizontal) to generate either the receiver function or the spectral ratio. In the autocorrelation approach presented in this study, we use, individually, vertical and horizontal records recorded on a similar set of stations as in Yan et al. (2018), to construct the vertical and horizontal autocorrelation stacks, which in turn feature reflection signals of P and S waves. Consequently, we can estimate the ice thickness using only vertical stacked autocorrelograms and the v_P/v_S ratio of the ice sheet at those recording sites when horizontal autocorrelograms are incorporated.

2. Data and Method

2.1. Data Collection

We collected broadband data recorded in Antarctica from the IRIS Data Center (Figure 1). There were 70 over-ice stations including two permanent stations QSPA (South Pole) and CCD (Concordia base; Wittlinger & Farra, 2012) whose data are publicly available during our access time in April 2017. The remainder belongs to three temporary experiments, that is, the Transantarctic Seismic Experiment (TAMSEIS; Lawrence et al., 2006), the Gambursev Seismic Experiment (GAMSEIS; Lloyd et al., 2013), and the Polar Observation Network (POLENET; Chaput et al., 2014; see Figure 1 for the location map). We retrieved three-component broadband data of teleseismic events with a magnitude criteria Mw ≥ 5.5 (Ekström et al., 2012) in period 2001–2003 for TAMSEIS and 2008–2012 for GAMSEIS and POLENET networks (see Table S1 in the supporting information for

a full list of stations). We excluded earthquakes that have epicentral distance closer than 30° to keep P wave incidences steep and ones that are in the distance range 95°–120° to avoid the diffraction of P waves at the core-mantle boundary. However, there is no selection criteria for earthquake depth. In practice, we used P waves propagating through the mantle in the epicentral distance range 30°–95° and PKIKP waves propagating through the Earth's core when the events are beyond 120°.

A visual inspection identifies seismograms with a high signal-to-noise ratio (SNR) around the P onset. Because of the use of P wave coda, the SNR in vertical seismograms is typically higher than on their horizontal counterparts. Thus, most stations have more vertical seismograms qualified for further analysis than the horizontal ones. Table S1 provides the number of seismograms for each station after data selection. We then concentrate on the time window of length 30 s starting 5 s ahead of the first P arrival predicted by the reference model AK135 (Kennett et al., 1995). All stations except CCD have the sampling rate at 40 samples per second; hence, we resample records of this station to the same rate. Finally, all horizontal components are rotated to the radial-transverse coordinate system. No prefiltering or instrument correction are required in this data preparation stage.

2.2. Spectral Whitening and Autocorrelation

Detailed description and demonstrating examples of the P wave coda autocorrelation can be found in Phạm and Tkalčić (2017). First, the selected wave forms were transformed to the spectral domain and then normalized by a spectral whitening operation. This operation is of a particular importance because it helps to mitigate the combined effects of earthquake source and propagating raypath, which usually cause a depletion of energy at the high end of the spectrum due to dissipation through the Earth interior. The whitening operation balances the contribution of all frequencies in the spectrum, so that it enhances high-frequency signals that are sensitive to the local structure. If $s_n(\omega)$ is an original complex spectrum of an input P wave coda record, the whitened spectrum $\widehat{s}_n$ is calculated as (Bensen et al., 2007),

$$\widehat{s}_n = \frac{s_n}{\frac{1}{2N+1}\sum_{j=n-N}^{n+N}|s_j|}, \tag{1}$$

where N specifies the number of points in the averaging weight of the amplitude spectrum $|s_j|$ in the denominator. The weight term, which is positive, is then divided from the original spectrum to normalize its amplitude but still preserve the original phase spectrum. For convenience, we can define the spectral whitening width $\Delta W = 2N \, \Delta f$ (Hz) where $\Delta f = 1/L$ is the discrete frequency step in which the seismogram length L is pre-fixed, for example, $L = 30$ s in this study.

Second, the autocorrelation in the spectral domain is the power of the whitened spectrum, namely,

$$a_n = \widehat{s}_n \cdot \widehat{s}_n^* = |\widehat{s}_n|^2. \tag{2}$$

The autocorrelation spectrum, a_n, is a purely real quantity since the phase spectrum is canceled by the self-conjugate multiplication. When returning to the time domain by an inverse Fourier transform, we keep the half of the symmetric autocorrelation function having positive delay time. This time series is then tapered with a cosine function to suppress the inherent central peak at time 0 s and subsequently filtered in an appropriate frequency band using a zero-phase Butterworth band-pass filter. We empirically find that the frequency band 1–5 Hz is suitable for the ice-bedrock system considered here. This frequency band corresponds to the wavelength 0.8–4.0 km given P wave speed in ice is 4 km/s. Autocorrelation of individual events is then stacked to enhance the SNR of the reflection signals and suppress incoherent features such as the effects of source time functions, earthquake depth phases, and source side scatterings; see section 6.3 (Phạm & Tkalčić, 2017) for more details.

Figure 2 presents autocorrelation results for the pilot station BYRD (see Figure 1) in West Antarctica, which was deployed on top of ~2.25-km-thick ice sheet (see Chaput et al., 2014, for receiver function results for this station). On the left panels are vertical and radial autocorrelations of P wave coda computed for individual earthquakes and plotted as functions of epicentral distance. We can identify negative signals (marked as 2p and 2s) prominent on most individual autocorrelograms at around 1 s that are associated to reflections from the ice-rock interface beneath the station. The signals align almost horizontally and do not show
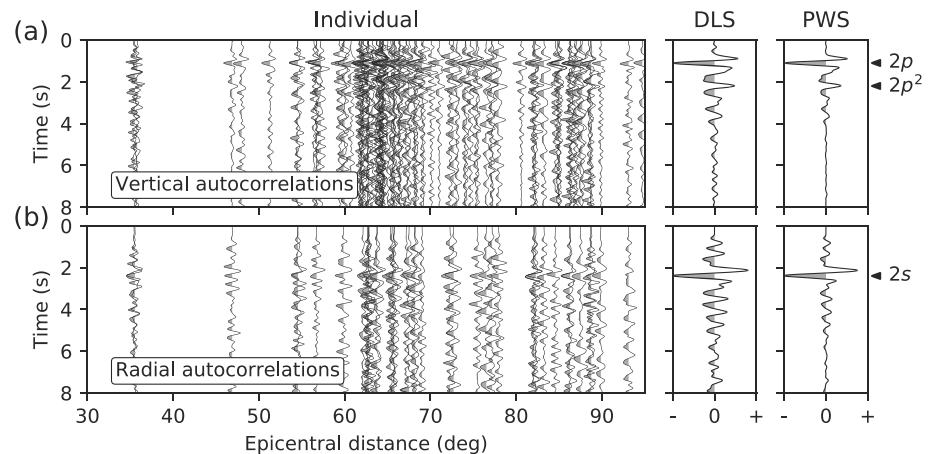
Figure 2. Example of (a) vertical and (b) radial individual autocorrelations and their linear (DLS) and phase-weighted stacks (PWS; Schimmel & Paulssen, 1997), computed for the pilot station, BYRD (80.02°S, 119.47°E—the big red triangle in Figure 1). Panels on the left show individual one-sided autocorrelations of teleseismic *P* codas as a function of epicentral distance after a taper function and a band-pass Butterworth filter of 1–5 Hz were applied. The spectral whitening width, ΔW, is 1.0 and 0.5 Hz for the vertical and radial autocorrelograms, respectively.

discernable dependence on epicentral distance. Due to the alignment, the peaks are markedly enhanced the autocorrelation stacks over all earthquakes. The middle and right panels of Figure 2 show results of the linear stacking and phase-weighted stacking methods. The latter stacking method is a nonlinear technique that utilizes the average phase among input traces as a coherency measurement to weight the linear stack (Schimmel & Paulssen, 1997); thus, it gives a better SNR to the reflection signals than the linear one. We use the phase-weighted stacking technique of order 1 to produce resulting autocorrelations in this paper, unless otherwise specified.
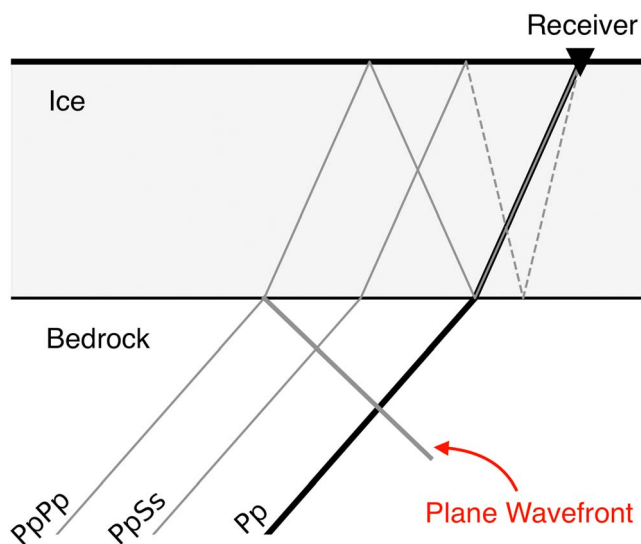

Figure 3. A schematic diagram illustrating the first-order approximation of seismic structure beneath a receiver installed on ice, consisting of a horizontal ice layer over a half-space bedrock. A plane *P* wavefront (gray thick line) illuminates the ice structure in a nearly vertical fashion. Different ray paths from the plane wave arrive to a receiver: *Pp* (black line) and *PpPp* and *PpSs* (gray lines). The naming convention of the reverberating arrivals is taken from Ammon (1991). Except for the first letter that indicates the initial *P* wave incidence to the ice-bedrock interface, the following lowercase and uppercase letters denote upward and downward legs reverberating in the ice layer. Solid and dashed lines represent *P* and *S* wave legs.

To interpret the reflection signals observed in Figure 2, we consider a simplified structure beneath a receiver with a homogeneous ice layer over a half-space bedrock in Figure 3. A plane *P* wave propagates to the receiver in a nearly vertical fashion. Because ground motions caused by the first *P* wave arrival (*Pp*) and its reverberating arrivals (e.g., *PpPp* and *PpPpPp*) are in the direction of propagation, they are dominant on the vertical component. Moreover, the arrivals are originated from a common seismic source and have similar propagating paths; thus, they result in the recurrence of similar wave form features in the vertical seismogram. Autocorrelation function contains correlation peaks that are generated due to the similarity of wave forms. A prominent peak, denoted as *2p* (Figure 2a), is contributed by a number of overlapping correlation peaks of arrival pairs that have other legs in common but differ only in two *P* legs in the ice layer, one upward and another downward, for example, *Pp* and *PpPp*, or *PpPp* and *PpPpPp*. In the following, we will refer to this peak as a single *P* wave reflection. It has negative amplitude because correlation pairs have opposite phases due to an additional surface reflection.

The above principle also explains the emergence of other correlation phases on vertical as well as on radial autocorrelations. A later correlation peak in the vertical autocorrelation stack (Figure 2a), denoted as *2p²*, is the correlation result of phase pairs that have two upward and two downward *P* legs in difference, for example, *Pp* and *PpPpPp*. This peak, which is then referred to as a double *P* wave reflection, has positive amplitude, because correlation pairs are in phase because of two additional surface reflections.

Similarly, ground motions of shear waves that are converted from the oblique incidence of the original plane *P* wave are perpendicular to the
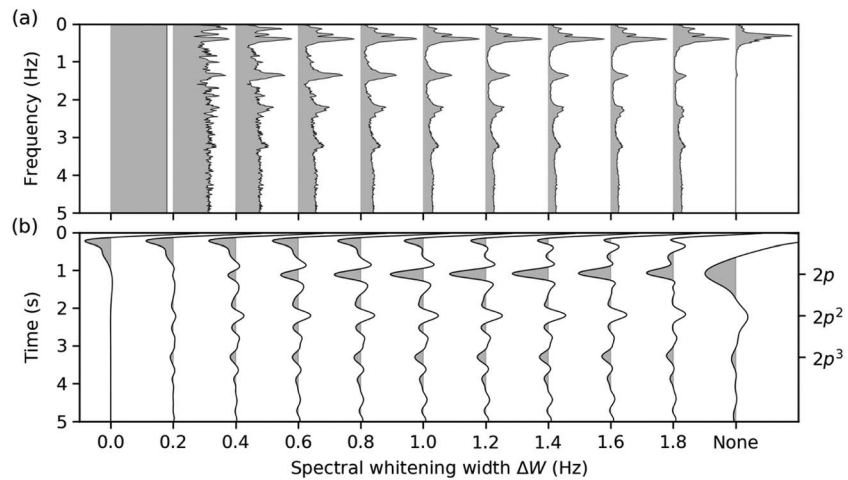
Figure 4. Effect of tuning spectral whitening width, ΔW, (see equation (1)) for the vertical-component autocorrelations, computed for the pilot station, BYRD. The wave form data set is identical to that shown in Figure 2a. (a) Linear stacks of power spectra and (b) corresponding temporal autocorrelations are computed for different whitening widths indicated along horizontal axis. "None" means that the autocorrelation is constructed without the spectral whitening. Results for the radial data set used in Figure 2b are shown in Figure S1.

propagation direction and so prominent in the radial component. A single reflection of shear waves, denoted as *2s*, is the correlation result of phase pairs that are different in two *S* wave legs within the ice layer, for example, *Pp* and *PpSs*. The *S* wave reflection signal also has negative amplitude (Figure 2b), as its compressional counterpart, due to one surface reflection difference between any contributing phase pair.

2.3. Selection of Spectral Whitening Width

It is noteworthy that the spectral whitening operation characterized in equation (1) is critical in the autocorrelation processing (Phạm & Tkalčić, 2017). A question arises on how we should choose its controlling parameter, the spectral whitening width ΔW, in order to recover effectively reflection signals. In a recent study, Oren and Nowack (2017) defined a similar whitening operation in which they used a Gaussian weighted filter rather than the unweighted averaging filter in this study to yield the weighting denominator. In that study, the Gaussian width, which is a counterpart of this study's spectral whitening width, is used to specify the smoothness of the weighting factor and hence results in spectral undulations to be recovered. Their study suggested that the Gaussian width that equals to the reciprocal of the two-way reflection time in the crust would produce high-quality autocorrelation results associated to the Moho discontinuity.

To provide insights on the selection of the whitening width ΔW, we consider resonance patterns recovered in a linear stack of whitened power spectra that are characterized in equation (2) as a function of different spectral widths (Figure 4a). The spectral stacks are equivalent to the temporal stacks in Figure 4b via an inverse Fourier transform because the Fourier transform is an additive operation (Stein & Wysession, 2003, ch. 6). When the whitening widths are larger than 0.4 Hz, regularly spacing resonance peaks up to ~3 Hz emerge in the whitened power stacks (Figure 4a). The peaks correspond to the reverberation of *P* waves in the ice. The spacing distance of the peaks (~0.85 Hz) is reciprocal to the vertical two-way travel time in the ice layer $\tau \approx 2H/v_P \approx 1.13$ s (where $H \approx 2.25$ km and $v_P \approx 4$ km/s). The spectral resonance pattern of a layer over a half-space configuration is theoretically derived in Appendix A1. Figure A1 shows the correspondence between the spacing of resonance peaks in the theoretical and empirical spectral responses. In the radial component corresponding shear waves, the resonance pattern can also be seen (see Figure S1) and their spacing is approximately twice denser than the vertical counterparts because the ratio between *P* wave and *S* wave speeds is ~2.

The spectral whitening in equation (1) is a mathematical function that features local spectral maxima in the vicinity of the spectral whitening width ΔW. Because the resonance peaks relating to the ice layer, equation (A8), are of our interest, the optimal width value should be chosen in correspondence to the spacing distance. Empirically, the range between one and two resonance spacing distances is the optimal range for

the width value, which is practically 0.8–1.6 and 0.4–0.8 Hz for the vertical and radial examples presented in Figures 4 and S1. This range is subjected to vary for other stations because it is inversely proportional to local ice thickness.

2.4. Oblique Move-Out

In a horizontal layer model, all reverberating ray paths retain the surface slowness from the original plane wave, β. This slowness can be determined as a function of epicentral distance and source depth. The delay time of the P wave reflection $2p$ is (e.g., Sun & Kennett, 2016)

$$t_{2p} = t_{PpPp} - t_{Pp} = 2H\sqrt{\frac{1}{v_P^2} - \beta^2} = \frac{2H\cos i_P}{v_P},$$

(3)

where H and v_P are the ice layer thickness and its compressional wave speed and i_P is the oblique angle of incidence at the surface. When the epicentral distance decreases, the P wave incidence deviates more from the vertical (i.e., larger i_P) and so the delay time t_{2p} decreases monotonously. The delay time gets its maximum at the vertical incidence, $2H/v_P$. Because we use the epicentral distance threshold of 30° (see section 2.1), which is equivalent to $i_P \approx 15°$, the delay time has the minimum of 95% of the vertical delay time for the P wave speed in ice ~4 km/s. The double reflection $2p^2$ delays are twice as large as the single one. The delay time for the shear wave reflection is also given by equation (3), but P wave speed and incident angle are replaced by the corresponding values for shear waves. Note that, in Figure 2, the dependence on ray parameter (or equivalently epicentral distance) of delay time (equation (3)) is negligible in the thin ice, since the delay time, $2H/v_P$, up to 4 s, is relatively small.

3. Results

### 3.1. Autocorrelation Results for Other Antarctic Ice Stations

Single-component autocorrelation stacks for other stations are presented in Figures 5 and S2. Table 1 lists the spectral whitening widths employed in the computation of the autocorrelation stacks. They are results of the visual comparison of autocorrelation wave forms for each station component that is similar to what is done in Figure 4. Most processed autocorrelograms represent a consistent reflection pattern with a prominent negative peak corresponding to the single reflection from the sharp ice-bedrock interface. The two-way reflection times in the vertical direction are then picked at the negative peaks. Component autocorrelations that do not show the reflection pattern for the range of whitening widths under consideration are rejected from further analysis and absent in Figures 5 and S2. Table S1 provides a list of selected and discarded station components. Among the discarded components, several have large numbers of utilized seismograms. For those, the poor quality of the autocorrelation stacks is likely due to the structural complexity within the ice layer and/or near the interface with bedrock.

Subsequently, we use the bootstrap resampling method (Efron & Tibshirani, 1991) to estimate the uncertainty of the time picks. The original collection of individual autocorrelations of each station component is resampled with replacement. Then reflection delays were automatically picked on the resampled stacks. The mean and standard deviation of 100 resampled picks represents the estimates of the two-way reflection time (t_{2x}) and error bound (δt_{2x}). When the estimated error bounds are under the sampling interval $\Delta t = 0.025$ s, we use the sampling step as the error bound (i.e., $\delta t_{2x} = \Delta t$). Overall, the picking procedure results in 62 time picks of P wave reflections and 33 time picks of S wave reflections, which are summarized in Table 1. In the next sections, we use the time picks to estimate ice sheet properties.

The mathematical equivalence between temporal reflection delays and spectral peaking spaces illustrated in Figures 4 and A1 suggests that these measurements in both domains can be used to infer the ice properties equivalently (equations (3) and (A8)). However, we prefer to measure time delays in practice because the time peaks are typically better defined in comparison with spectral peaks in most cases. Figure S1 presents an example in which the quality of the spectral peaks is poorer than in the temporal counterparts.

3.2. *P* Wave Reflectivity and Ice Thickness Estimates

First, we convert the time picks of P wave reflections t_{2p} to ice thickness estimates,
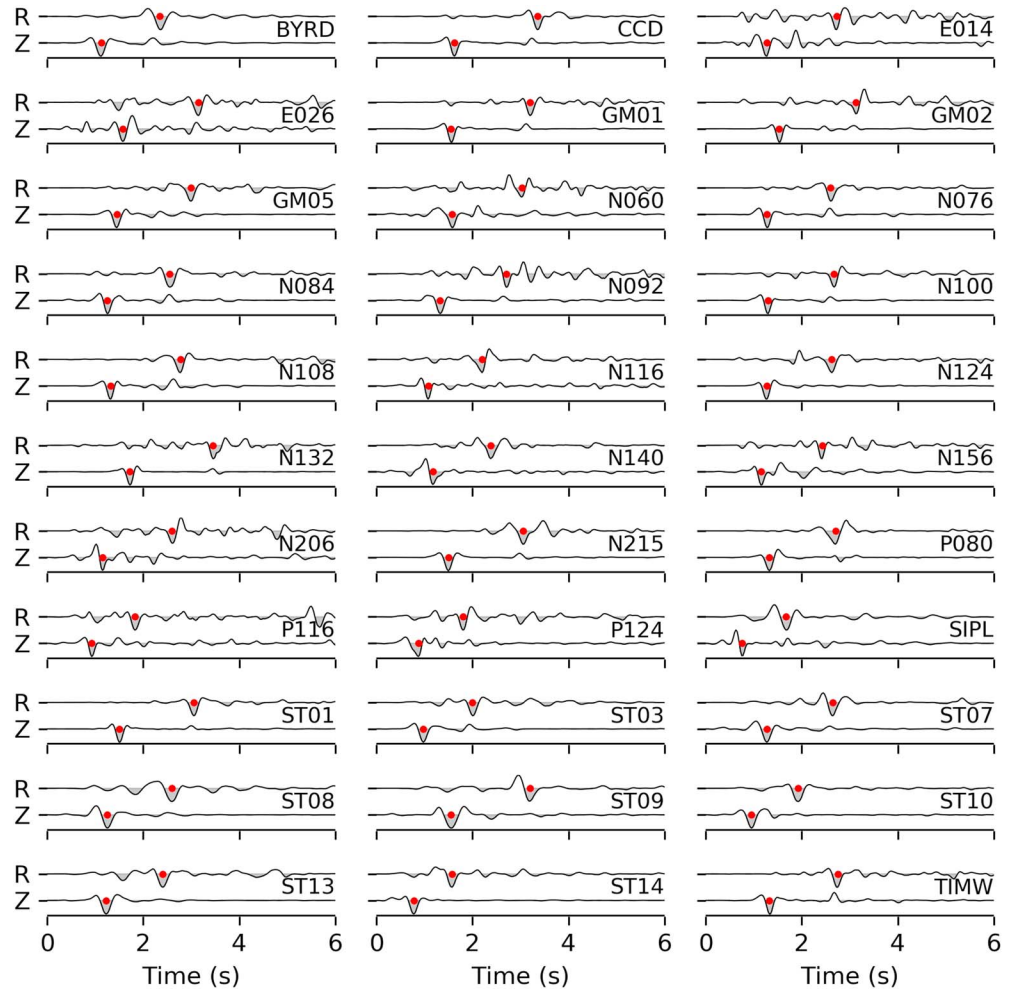
Figure 5. Autocorrelation stacks for 33 stations of which both components show good signal-to-noise ratio (see section 3.1). In each station panel, the bottom and top traces are vertical (Z) and radial (R) autocorrelograms. Red dots indicate time picks of *P* or *S* reflections. Autocorrelation stacks for 29 stations that have only a good-quality vertical component are shown in Figure S2.

$$H \approx \frac{t_{2p} v_P}{2}. \tag{4}$$

The conversion is performed using an approximation of a homogeneous *P* wave speed of $v_P = 3{,}900$ m/s (Kohnen, 1974). This empirical value is consistent with what is derived from elastic parameters of single ice crystals (Gagnon et al., 1988; Wittlinger & Farra, 2012). Because the speed also depends on temperature and pressure applied on the ice column, we set the velocity uncertainty of $\delta v_P = 100$ m/s (Kohnen, 1974). As a consequence, the error bound δH of the thickness estimate is propagated from the error bounds of the time pick, δt_{2P}, and *P* wave speed, δv_P,

$$\delta H \approx \frac{\left(v_P \delta t_{2p} + t_{2p} \delta v_P \right)}{2}. \tag{5}$$

Figure 6 shows the match of these measurements along two profiles (lines AB and CD in Figure 1), and Figure 7 shows a comparison of the whole set of estimates. Our thickness estimates utilizing passive seismic data show an excellent agreement with the BEDMAP2 (Fretwell et al., 2013), which corroborates the autocorrelation results. However, large differences (>1,500 m) can be seen at the locations of three stations: E014, E026, and SWEI (three dark blue dots in Figure 7). We speculate that because the first two stations are

Table 1
Ice Thickness and v_P/v_S Results Obtained in This Study

No.	Station	Whitening width (Hz)	P wave reflection (s)	S wave reflection (s)	BEDMAP2 (m)	Estimated thickness (m)	v_P/v_S
1	BYRD	0.75	1.15 ± 0.03	2.36 ± 0.03	2,185	2,242 ± 106	2.05 ± 0.09
2	CCD	0.75	1.65 ± 0.03	3.35 ± 0.03	3,177	3,217 ± 131	2.03 ± 0.13
3	E014	0.75	1.27 ± 0.03	2.71 ± 0.03	693	2,476 ± 112	2.13 ± 0.1
4	E026	0.75	1.58 ± 0.03	3.15 ± 0.03	1,382	3,081 ± 127	1.99 ± 0.12
5	GM01	0.50	1.56 ± 0.03	3.21 ± 0.03	3,096	3,042 ± 126	2.06 ± 0.12
6	GM02	0.50	1.54 ± 0.03	3.13 ± 0.03	2,810	3,003 ± 125	2.03 ± 0.12
7	GM05	0.50	1.45 ± 0.03	3 ± 0.03	3,460	2,827 ± 121	2.07 ± 0.11
8	N060	0.75	1.58 ± 0.03	3.01 ± 0.05	2,833	3,081 ± 127	1.91 ± 0.15
9	N076	0.75	1.28 ± 0.03	2.6 ± 0.03	2,455	2,496 ± 112	2.03 ± 0.1
10	N084	0.75	1.28 ± 0.03	2.56 ± 0.03	2,473	2,496 ± 112	2 ± 0.1
11	N092	0.75	1.33 ± 0.03	2.71 ± 0.03	2,634	2,593 ± 115	2.04 ± 0.11
12	N100	0.50	1.3 ± 0.03	2.68 ± 0.03	2,691	2,535 ± 113	2.06 ± 0.1
13	N108	0.50	1.33 ± 0.03	2.77 ± 0.03	2,443	2,593 ± 115	2.08 ± 0.1
14	N116	0.75	1.1 ± 0.03	2.19 ± 0.03	2,491	2,145 ± 103	1.99 ± 0.08
15	N124	0.50	1.27 ± 0.03	2.62 ± 0.03	2,409	2,476 ± 112	2.06 ± 0.1
16	N132	0.50	1.73 ± 0.03	3.48 ± 0.04	3,238	3,373 ± 135	2.01 ± 0.16
17	N140	0.75	1.17 ± 0.03	2.39 ± 0.03	2,806	2,281 ± 107	2.04 ± 0.09
18	N156	1.00	1.15 ± 0.03	2.42 ± 0.03	2,539	2,242 ± 106	2.1 ± 0.09
19	N206	1.00	1.15 ± 0.03	2.61 ± 0.03	2,970	2,242 ± 106	2.27 ± 0.09
20	N215	0.50	1.52 ± 0.03	3.06 ± 0.03	3,470	2,964 ± 124	2.01 ± 0.11
21	P080	0.50	1.33 ± 0.03	2.69 ± 0.03	2,500	2,593 ± 115	2.02 ± 0.1
22	P116	1.00	0.93 ± 0.03	1.83 ± 0.04	1,995	1,813 ± 95	1.97 ± 0.08
23	P124	1.00	0.9 ± 0.03	1.81 ± 0.03	1,496	1,755 ± 93	2.01 ± 0.07
24	SIPL	1.25	0.76 ± 0.03	1.68 ± 0.03	990	1,482 ± 86	2.21 ± 0.06
25	ST01	0.50	1.53 ± 0.03	3.06 ± 0.03	2,943	2,983 ± 125	2 ± 0.11
26	ST03	1.00	0.98 ± 0.03	2.01 ± 0.03	1,951	1,911 ± 97	2.05 ± 0.07
27	ST07	0.75	1.27 ± 0.03	2.64 ± 0.03	2,489	2,476 ± 112	2.08 ± 0.1
28	ST08	0.75	1.28 ± 0.03	2.6 ± 0.03	2,187	2,496 ± 112	2.03 ± 0.1
29	ST09	0.75	1.56 ± 0.03	3.19 ± 0.03	2,317	3,042 ± 126	2.04 ± 0.12
30	ST10	0.75	0.95 ± 0.03	1.92 ± 0.03	1,243	1,852 ± 96	2.02 ± 0.07
31	ST13	0.75	1.23 ± 0.03	2.41 ± 0.03	1,940	2,398 ± 110	1.96 ± 0.09
32	ST14	1.25	0.78 ± 0.03	1.57 ± 0.03	1,549	1,521 ± 87	2.01 ± 0.06
33	TIMW	0.50	1.33 ± 0.03	2.74 ± 0.03	2,572	2,593 ± 115	2.06 ± 0.1
34	BENN	1.50	1.02 ± 0.03	—	1,552	1,989 ± 99	—
35	DNTW	0.75	0.9 ± 0.03	—	2,144	1,755 ± 93	—
36	E020	0.75	0.73 ± 0.03	—	1,742	1,423 ± 85	—
37	E024	1.25	1.02 ± 0.03	—	1,904	1,989 ± 99	—
38	E028	1.25	1.09 ± 0.03	—	1,640	2,125 ± 103	—
39	GM03	0.50	1.65 ± 0.03	—	2,529	3,217 ± 131	—
40	GM04	0.50	1.64 ± 0.03	—	2,803	3,198 ± 130	—
41	GM06	0.50	1.65 ± 0.03	—	3,456	3,217 ± 131	—
42	GM07	0.50	1.65 ± 0.03	—	3,051	3,217 ± 131	—
43	KOLR	0.75	1.53 ± 0.03	—	2,350	2,983 ± 125	—
44	N020	1.00	1.61 ± 0.03	—	1,788	3,139 ± 129	—
45	N044	1.00	1.34 ± 0.03	—	2,242	2,613 ± 115	—
46	N068	0.50	1.28 ± 0.03	—	2,890	2,496 ± 112	—
47	N148	0.50	1.4 ± 0.03	—	2,901	2,730 ± 118	—
48	N165	0.75	1.61 ± 0.03	—	2,810	3,139 ± 129	—
49	N173	0.75	1.39 ± 0.03	—	2,407	2,710 ± 118	—
50	N182	0.50	1.52 ± 0.03	—	2,413	2,964 ± 124	—
51	N190	0.50	1.05 ± 0.03	—	3,007	2,047 ± 101	—
52	N198	0.50	1.33 ± 0.03	—	3,322	2,593 ± 115	—
53	P061	0.50	0.82 ± 0.03	—	3,158	1,599 ± 89	—
54	P071	0.75	1.18 ± 0.03	—	2,279	2,301 ± 107	—
55	P090	0.50	1.22 ± 0.03	—	2,343	2,379 ± 109	—
56	QSPA	1.00	1.28 ± 0.03	—	2,815	2,496 ± 112	—
57	ST02	0.75	1.77 ± 0.03	—	2,126	3,451 ± 137	—
58	ST04	0.50	1.48 ± 0.03	—	3,140	2,886 ± 122	—
59	ST06	0.50	2.33 ± 0.03	—	2,668	4,543 ± 165	—
60	SWEI	0.50	1.48 ± 0.03	—	2,840	2,886 ± 122	—

Table 1 *(continued)*

No.	Station	Whitening width (Hz)	*P* wave reflection (s)	*S* wave reflection (s)	BEDMAP2 (m)	Estimated thickness (m)	v_P/v_S
61	UPTW	0.50	1.68 ± 0.03	—	2,650	3,276 ± 132	—
62	WAIS	0.50	1.48 ± 0.03	—	3,311	2,886 ± 122	—

Note. Empirically chosen values of the spectral whitening width, ΔW, for each station are listed in column 3. *P* and *S* wave reflection arrival times picked on vertical and radial autocorrelation stacks are listed in columns 4 and 5. Ice thickness data extracted from the BEDMAP2 database (Fretwell et al., 2013) are listed in column 6 for reference. Estimated measurements of ice thickness and v_P/v_S ratio in this study are listed in columns 7 and 8. Dashed lines in empty cells mean that there are no available measurements.

located in a mountainous area of the Transantarctic Mountains (Hansen et al., 2009), the thickness of the ice cover could possibly vary significantly at short distances due to sub-ice topography. Thus, the interpolation over a number of directly measured points as implemented in the BEDMAP2 data set may underestimate the true ice thickness.

3.3. *S* Wave Reflectivity and Estimating v_P/v_S Ratio

The autocorrelation method has so far been applied widely to vertical records to extract the *P* wave reflectivity of the local structure beneath a seismic station (e.g., Kennett, 2015; Kennett et al., 2015; Saygin et al., 2017). However, there are limited studies reporting on extracting *S* wave reflections by the same technique. In one of the pioneering autocorrelation works, Tibuleac and von Seggern (2012) constructed daily stacked
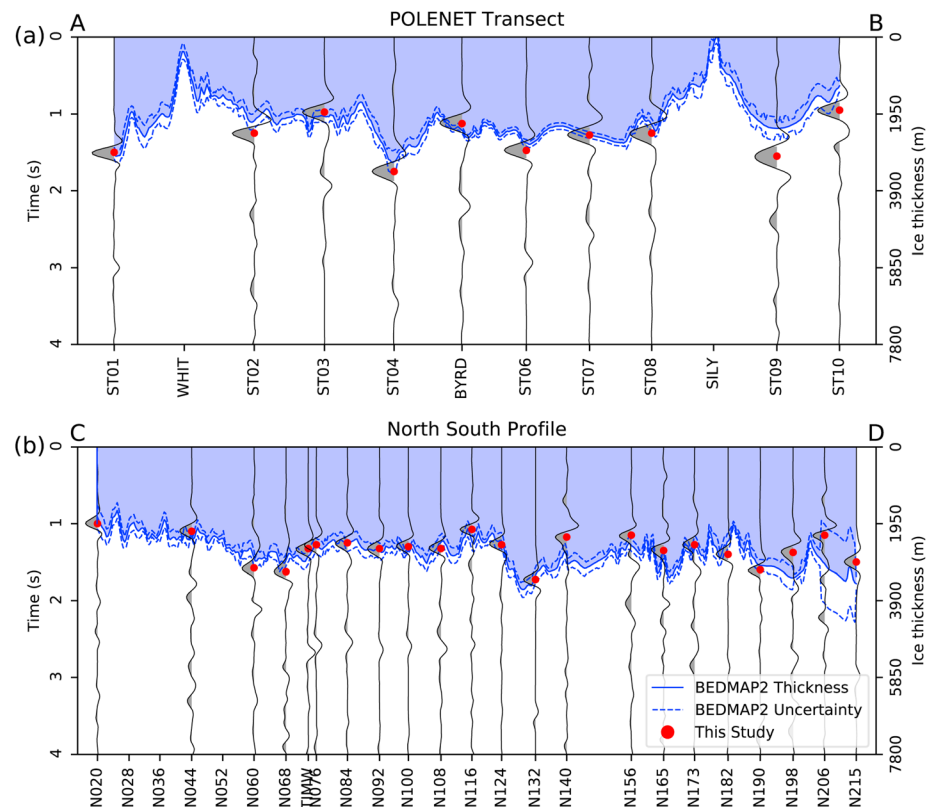
Figure 6. Linear profiles AB and CD (see Figure 1) of vertical autocorrelation stacks. (a) Line AB consists of temporary deployments of the POLENET. (b) Line CD consists of stations of the GAMSEIS and TAMSEIS networks. Vertical autocorrelation stacks (gray traces) are arranged by their relative distances from the beginning of each line. Blue solid and dashed lines represent the ice thickness extracted from the BEDMAP2 database (Fretwell et al., 2013) and its uncertainty bound along the profiles. Red dots indicate the *P* wave reflection arrival picks on the vertical autocorrelations. The conversion between the reflection time and the ice thickness is performed using a homogeneous *P* wave speed in ice of 3.9 km/s (Kohnen, 1974).
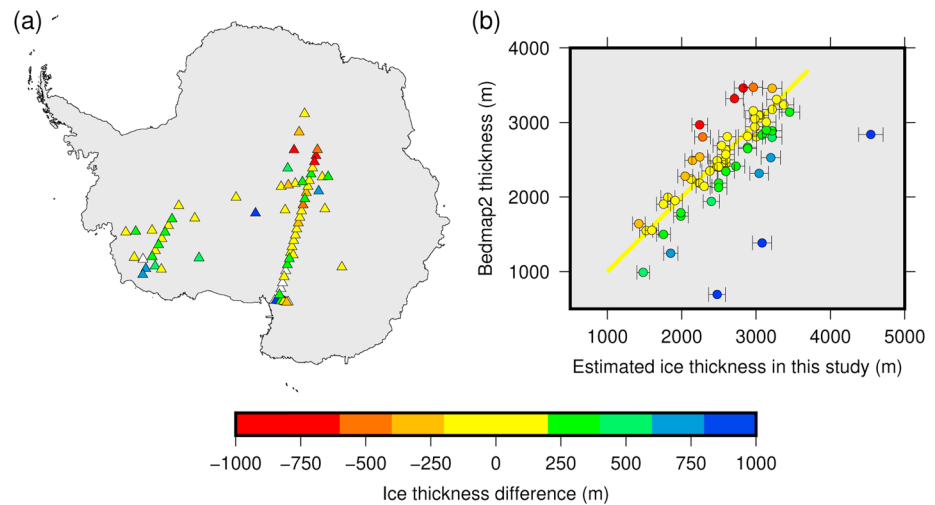
Figure 7. A comparison of the estimated ice thickness in this study with the BEDMAP2 results (Fretwell et al., 2013). (a) Location maps of stations used in this study. Colors show the difference between the estimates and the BEDMAP2 ice thickness. Stations in white had noisy autocorrelation stacks and were rejected. (b) A comparison of the estimated ice thickness on the horizontal axis and the BEDMAP2 ice thickness on the vertical axis. A conversion from the travel time to the ice thickness uses a homogeneous P wave velocity of 3.9 km/s (Kohnen, 1974).

autocorrelograms of all three broadband components. They demonstrated observations of P and S wave reflections on each recording component (i.e., BHZ, BHN, and BHE) from a sharp Moho discontinuity in central United States. Recently, Oren and Nowack (2017) confirmed the observation with an improved data processing applied to vertical data of several stations in the same region.

The use of nearly vertical plane waves results in the separation of direct P and converted S waves recorded on vertical and horizontal components. By using radial seismograms, we obtain S wave reflectivity records for 33 stations (Figure 5). Assuming that the ice is well represented by a homogeneous layer, the ratio of P and S delay times represents the wave speed ratio, v_P/v_S,

$$\kappa = \frac{t_{2s}}{t_{2p}}. \tag{6}$$

It is noteworthy that considering S wave reflections is a novel way to estimate S wave velocity, or the v_P/v_S ratio, of ice in the field. These measurements have been rarely obtained from acoustic sources in active experiments (Wittlinger & Farra, 2015). The error bound of the v_P/v_S ratio is propagated from the time pick error bounds as

$$\delta\kappa = t_{2s}\delta t_{2p} + t_{2p}\delta t_{2s}. \tag{7}$$

The estimated v_P/v_S ratios, shown in Figure 8, are consistent with empirical values of ~2 for the ratio in ice (Kohnen, 1974) except for the two outliers at stations SIPL and N206 (~2.2). The abnormal values of v_S at the two stations can also be seen in the autocorrelation stacks of the transverse component (Figures S3 and S4). Further insights in explaining the abnormal values for these two stations are beyond the scope of this study.

4. Discussion

The recurrence of energy due to reflection is crucial in extracting body waves via correlation techniques (Wapenaar et al., 2010); however, we consider a possibility that some boundaries will stay hidden to teleseismic frequencies. Zhan et al. (2010) explained the observation of the Moho-reflected shear waves (SmS) beneath the Kimberley craton in South Africa in terms of postcritical reflections in their application of ambient noise cross-correlation. When the interstation distance vanishes, a cross-correlation becomes an
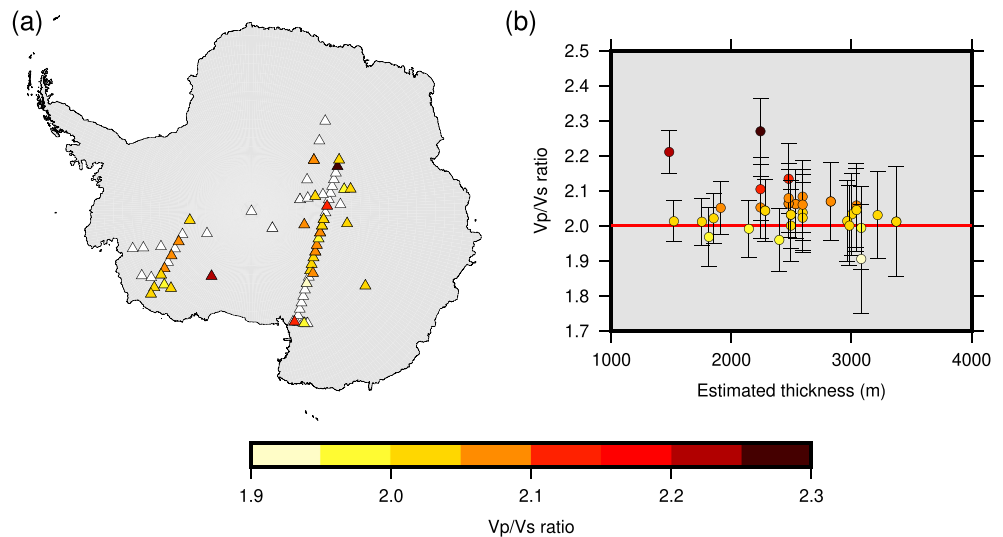
Figure 8. Point measurements of v_P/v_S ratio. (a) Location map of the stations used. Colors show the estimated values. Stations for which the measurements were not reliable are shown in white. (b) v_P/v_S ratios against estimated ice thickness. Error bars show the uncertainties of the measurements, which are propagated from the time-pick uncertainties. Red line shows "standard" value of $v_P/v_S \approx 2$ in ice (Kohnen, 1974).

autocorrelation, and the emergence of reflected signals relies on precritical reflection due to the fact that the angle of incidence is close to a normal incidence on an interface (Gorbatov et al., 2013). For a precritical reflection regime, it is the acoustic impedance contrast, the product of density and velocity, rather than just the velocity jump that determines the reflectivity efficiency of a discontinuity. Thus, an interface between two materials that have similar acoustic impedance contrast is transparent to incident waves (see Appendix A2).

To demonstrate the effect of "transparency," we consider a configuration of two seismic media with similar acoustic impedances that can be encountered in the subglacial contexts (Figure 9). Several studies have shown the existence of a sedimentary layer sandwiched in between the ice cover and the rocky basement in several places in Antarctica (e.g., Anandakrishnan & Winberry, 2004; Chaput et al., 2014). Those studies suggested that sedimentary rocks can have P wave velocity varying from 2 to 2.5 km/s, density of ~2 g/cm^3, and the Poisson's ratio varying from 0.2 to 0.4. Such a low P wave velocity is hypothesized to facilitate fast ice flows (Anandakrishnan & Winberry, 2004). Figure 9 shows synthetic vertical and radial autocorrelograms computed for the ice/sediment/rock model where the Poisson's ratio is fixed to 0.33 (or equivalently v_P/v_S~2) as in the studies mentioned above. For details of the synthetic experiment setup we refer the reader to section 4 (Phạm & Tkalčić, 2017). Although the sedimentary layer is a pronounced low-velocity zone having ~50% velocity reduction relative to ice, the autocorrelograms show no evidence for the ice-sediment interface due to its "transparency." Thus, the reflections undertake prominently at the sediment base instead of the ice base. This ambiguity would cause the deviation of the estimated ice thickness (and v_P/v_S ratio) from the true values of the ice sheet. In particular, the potential discrepancy can be up to two times of the sediment thickness since P wave speed is approximately twice faster in ice than in the sediment. This effect could possibly explain three outliers seen as three dark blue dots in Figure 7.

It is interesting to comment on the similarity between the autocorrelation and the spectral ratio (H/V) methods (e.g., Seht & Wohlenberg, 1999), both of which can be used to characterize site effects of thin ice or sediment layers (e.g., Yan et al., 2018). Spectral ratios are constructed by dividing horizontal to vertical amplitude spectra of ambient noise and stacking over multiple record segments. The spectral ratio stack features resonance peaks of near-vertically reverberating S wave energy contained in the noise (e.g., Seht & Wohlenberg, 1999). In a similar way, the spectral whitening operation (equation (1)) presents an effective means of revealing not only the fundamental mode but also several overtones of reverberating energy from teleseismic earthquakes (Figures 4 and S1), which are then equivalent to the reflection signals seen in the
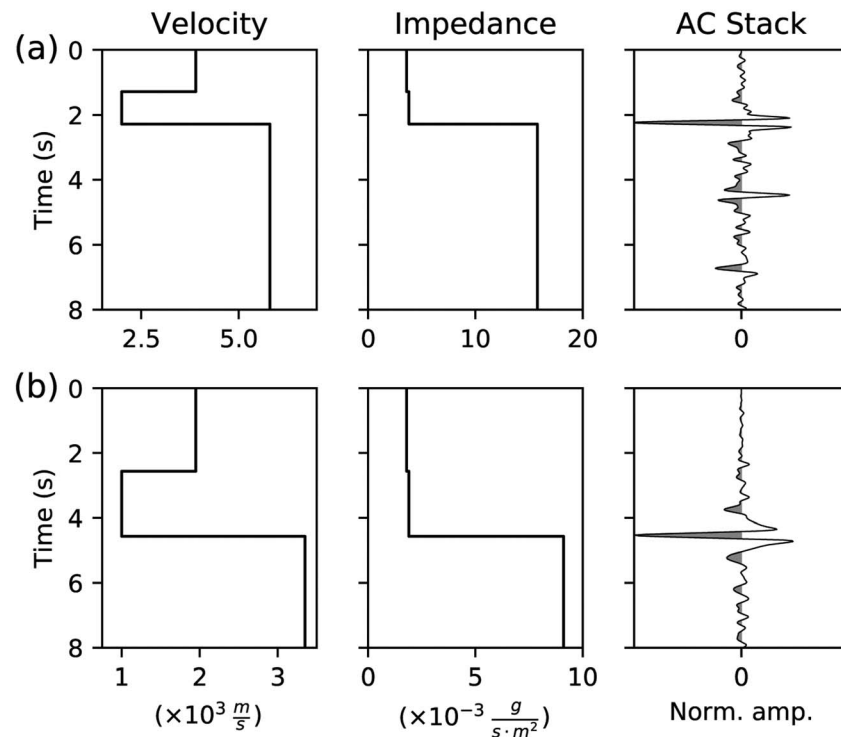
Figure 9. Effect of "a transparent" subglacial sedimentary layer on (a) vertical and (b) radial autocorrelation stacks. Velocity (left) and impedance profiles (middle) are plotted against the two-way vertical reflection delays. Right panels show synthetic autocorrelation stacks.

time domain. Furthermore, autocorrelations reveal resonance peaks relating to P and S waves for vertical and horizontal components separately.

In this study, we use relatively short wave forms of 30 s that include the P wave arrival itself. This particular portion of earthquake wave forms, which is termed P wave coda (e.g., Paulssen et al., 1993), contains the P onset and its following reverberations at the subsurface discontinuities. The autocorrelation function reveals the recurrence of the first arrival through its similarity with the reverberated arrivals. Thus, the inclusion of P wave signal is essential in our method. This differs from other kinds of coda studies, such as ambient noise applications that consider the direct arrivals as "contaminated signals" (e.g., Snieder & Larose, 2013).

We speculate that the P wave coda window length of 30 s could be expanded to obtain more robust auto-correlation stacks. The source-side reflections, for example, pP or sP, which have similar ray parameters to the main arrival could also be included. On the one hand, the source side effects are likely to be destructively canceled in autocorrelation stacks of earthquakes originating at various depths and in different geological settings (Phạm & Tkalčić, 2017). On the other hand, the receiver-side signals induced by the main arrival and the source reflections will be constructively enhanced due to the fact that they have similar oblique move-outs (see section 2.4 and equation (3)). However, the mentioned P wave coda window cannot be too long in order to avoid the interference of later primary phases arriving with different ray parameters, for example, PP and PS, because of the difference in oblique move-outs outs can deteriorate the constructive stack.

In this study, we rely on a working assumption that ice is isotropic. This assumption is not always valid given that a single ice crystal is anisotropic with S wave 17% slower and P wave 7% faster in the c-axis direction rela-tive to the perpendicular direction (e.g., Gagnon et al., 1988; Wittlinger & Farra, 2012). At the macroscopic scale, ice is generally considered isotropic because the c-axes are randomly oriented. However, the anisotro-pic properties can be significant if there is a preferential orientation of the c-axes. The preferential orientation can be forced by long-term pressure caused by self-gravity of the ice layer (e.g., Wittlinger & Farra, 2012) or by flow of ice (e.g., Anandakrishnan & Winberry, 2004), which can align the c-axes vertically or horizontally,

respectively. With further refinement of the autocorrelation method, the anisotropic properties, especially *S* wave anisotropy which is more significant than that of *P* waves, can be investigated in future studies.

The main limitation of the autocorrelation method presented in this study stems from the use of wave forms generated by major earthquakes ($M_w \geq 5.5$). In order to have enough data for analyses, seismic stations need to be deployed long enough (in order of several months to years). However, long deployments are not always available in a remote area such as Antarctica due to problems of logistics and maintenance. To overcome the problem related to a small population of major earthquakes, a possible approach could be to utilize continuous ambient seismic noise (Diez et al., 2016; Saygin et al., 2017; Zhan et al., 2014) or coda wave forms of other primary phases, rather than the first *P* arrival, such as *PP*, *PcP*, or *S* waves. An alternative possibility is to exploit wave form data of many smaller earthquakes, which occurs more frequently around the globe, because the stacking procedure over a large number of autocorrelations could enhance weak signals to the same quality as using several large events.

5. Concluding Remarks

In summary, we have presented a successful application of the autocorrelation technique utilizing *P* wave coda wave forms (Phạm & Tkalčić, 2017) to map the shallow ice-bedrock interface beneath a large number of ice stations in Antarctica. Wave forms of teleseismic earthquakes are used to provide nearly vertical illumination of the structures. The data processing employs the spectral whitening on individual wave forms before computing the autocorrelations. Vertical and radial stacked autocorrelograms represent the reflectivity of *P* and *S* waves. Results of thickness and v_P/v_S ratio are in a good agreement with the current knowledge of the Antarctic ice sheet from independent studies.

The autocorrelation method relying passive seismic data could have a wide-range potential in seismological studies of the polar regions. First, the method provides another source of reliable estimates of ice properties in a high resolution that can complement active source studies, which are often more expensive measurements (e.g., radio-echo sounding). Potential applications may be explored in Antarctica, Arctic, Greenland, and in future space missions to icy planets (e.g., Schenk, 2002). More importantly, a local seismic structure of ice beneath a recording station is a parameter of interest in seismological applications that target subglacial crustal imaging (e.g., Hansen et al., 2009, 2010; Ramirez et al., 2016) and is complementary to the values available in comprehensive ice thickness databases (Fretwell et al., 2013; Lythe et al., 2001). Furthermore, the ability to extract both *P* and *S* wave reflectivity and derive the speed ratio v_P/v_S is of a broad interest for future glacial studies because it overcomes the lack of field measurements that are sensitive to shear properties of ice.

The successful application in the ice environment presented here opens up a way to resolve other extreme geological settings where a shallow, distinguished seismic layer is present, such as sediments or permafrost. The autocorrelation method improves the resolution on the layer thickness and provides new constraints on the bulk wave speed ratio in the layer.

## Appendix A: Analytical Reflection Responses in Stratified Media

A1. A Layer Over a Half-Space

We present an explicit solution for a simplified acoustic structure of the reflection problem in the original work by Claerbout (1968). A stratified media beneath a recording station consists of a layer over a half-space, as in Figure A1a. An impulsive plane wave is incident to the base of the layer and propagates vertically upward to the station on the surface. In the spectral domain, the impulsive wave is represented by a unity function. The reflection coefficient *r* at the interface of a wave propagating downward from medium 1 to medium 2 is given by (Stein & Wysession, 2003, p. 76)

$$r = \frac{\rho_1 v_1 - \rho_2 v_2}{\rho_1 v_1 + \rho_2 v_2}, \tag{A1}$$

where (ρ_1, v_1) and (ρ_2, v_2) are the densities and the wave speed parameters corresponding to the layer and the half-space, respectively. The corresponding transmission coefficient *t* is
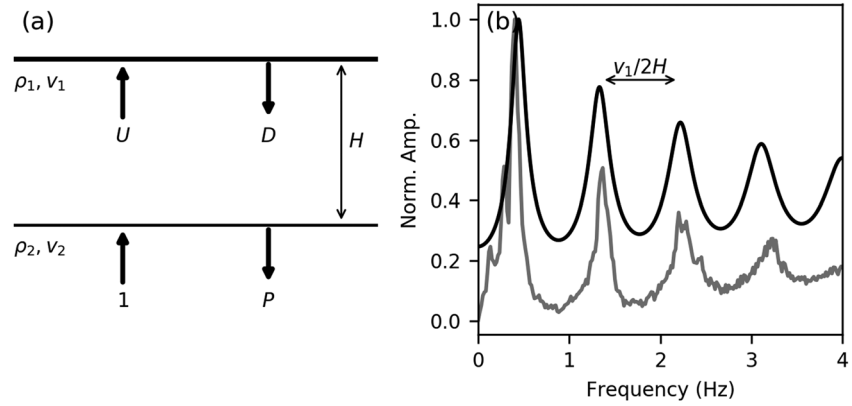
Figure A1. Setup of the reflection problem. (a) Simplified acoustic structure, characterized by density, ρ, and wave speed, v, consisting of a layer over a half-space. Bold arrows indicate direction of wave vectors in the layered medium. An impulse that is incident beneath the interface is a unity function in the frequency domain, and P represents the wave vector that propagates downward to the half-space. U and D represent the spectra of upward and downward waves at the free surface. (b) A comparison of theoretical spectral response (black line) and empirical spectral response (gray line) computed for the vertical seismograms of the pilot station, BYRD. The theoretical response is given by equation (A6) for the case of ice thickness, $H = 2.24$ km (see Table 1) and the wave speed, $v_1 = 3.9$ km/s. The empirical response is constructed using the whitening width value, $\Delta W = 1$ Hz (equation (1)), as shown in Figure 4a.

$$t = 1 + r. \tag{A2}$$

Let U, D represent the spectra of upward and downward waves at the free surface induced by the impulse, and P is the wave propagating downward in the half-space. A transfer function that relates their counterparts at the interface (see Figure A1; Claerbout, 1968) is given by

$$\begin{bmatrix} U \\ D \end{bmatrix} = \frac{1}{wt} \begin{bmatrix} z & zr \\ r & 1 \end{bmatrix} \begin{bmatrix} 1 \\ P \end{bmatrix}, \tag{A3}$$

in which $z = e^{i\omega(\tau + i \cdot Q)}$ and $w = z^{1/2}$ represent the propagation in time, where $\tau = 2H/v_1$ is the two-way travel time in the layer and Q is the attenuation quality factor in the layer. Multiplying with w or z in the frequency domain is equivalent to delaying the signals by $\tau/2$ and τ in the time domain.

At the free surface the reflection is perfect, so the upward and downward responses, U, D, are equal. Let $X = U = D$ be the response recorded by the surface recorder. Equation (A3) becomes

$$\begin{bmatrix} X \\ X \end{bmatrix} = \frac{1}{wt} \begin{bmatrix} z & zr \\ r & 1 \end{bmatrix} \begin{bmatrix} 1 \\ P \end{bmatrix}. \tag{A4}$$

To solve for X, we compute the inverse of the transfer matrix

$$\frac{1+r}{1-r} \begin{bmatrix} 1 & -zr \\ -r & z \end{bmatrix} \begin{bmatrix} X \\ X \end{bmatrix} = \begin{bmatrix} 1 \\ P \end{bmatrix}, \tag{A5}$$

and thus

$$X = \frac{1-r}{1+r} \cdot \frac{1}{1-zr} = \frac{1-r}{1+r} \cdot \frac{1}{1 - re^{i\omega(\tau + i \cdot Q)}}. \tag{A6}$$

The autocorrelation cancels the phase spectrum and retains the square of the amplitude spectrum,

$$|X| = \frac{1-r}{1+r} \cdot \frac{1}{\sqrt{1 + (re^{-\omega Q})^2 - 2re^{-\omega Q} \cos\omega\tau}}. \tag{A7}$$

The amplitude spectrum peaks at angular frequencies, ω_n, that minimize the denominator. In case of an ice layer over a half-space considered in this study, provided $r < 0$, the peak angular frequencies satisfy $\cos\omega_n\tau = -1$ or $\omega_n\tau = \pi + 2n\pi$ ($n = 0, 1, 2, \ldots$). The resonance frequencies are

$$f_n = \frac{\omega_n}{2\pi} = \left(n + \frac{1}{2}\right)\cdot\frac{1}{\tau} \tag{A8}$$

Figure A1b graphically illustrates the amplitude spectrum $|X|$ in the frequency domain with the resonance peaks identified by equation (A8). The spacing between peaks is inversely proportional to the two-way travel time within the layer.

The spacing of the peak is due to the positive jump of acoustic impedance downward. In case the acoustic impedance is negative, the reflection coefficient is positive, the spacing of the frequency resonance peaks are then arranged by $f_n = n/\tau$, and the polarity of the first reflection is positive.

A2. Two Layers Over a Half-Space

Let us consider a model consisting of multiple layers over a half-space. As in equation (A1), the reflection coefficient, r_i, of a downward wave at the interface between medium i and medium $i + 1$ is

$$r_i = \frac{\rho_i v_i - \rho_{i+1} v_{i+1}}{\rho_i v_i + \rho_{i+1} v_{i+1}}, \tag{A9}$$

where ρ_i and v_i are density and wave speed in the ith layer and the transmission coefficient is given by $t_i = 1 + r_i$. The generalized transfer function between two consecutive interfaces, similarly to equation (A3), is

$$\begin{bmatrix} U_i \\ D_i \end{bmatrix} = \frac{1}{w_i t_i} \begin{bmatrix} z_i & z_i r_i \\ r_i & 1 \end{bmatrix} \begin{bmatrix} U_{i+1} \\ D_{i+1} \end{bmatrix}, \tag{A10}$$

where w_i and z_i also represent the temporal propagation terms.

In a model having two layers over a half-space, the spectral response at surface, X, induced by an impulse that is incident at the half-space, solves the following matrix equation:

$$\begin{bmatrix} X \\ X \end{bmatrix} = \left(\frac{1}{w_1 t_1}\begin{bmatrix} z_1 & z_1 r_1 \\ r_1 & 1 \end{bmatrix}\right)\left(\frac{1}{w_2 t_2}\begin{bmatrix} z_2 & z_2 r_2 \\ r_2 & 1 \end{bmatrix}\right)\begin{bmatrix} 1 \\ P \end{bmatrix}. \tag{A11}$$

By computing the inverse of the transfer matrices as in equation (A5), we have

$$X = \frac{1 - r_1}{1 + r_1}\frac{1 - r_2}{1 + r_2}\frac{1}{1 - r_1 z_1 + r_1 r_2 z_2 - r_2 z_1 z_2}. \tag{A12}$$

The response consists of terms that represent the reverberations in layer 1: $-r_1 z_1$, in layer 2: $r_1 r_2 z_2$, and over the interface of both layers: $-r_2 z_1 z_2$. When the acoustic impedances over the intermediate interface are equal, $r_1 = 0$, the spectral response at surface, X, is identical to the case of only a layer over a half-space (equation (A6)), in which the propagation term represents the total travel time in both layers,

$$X = \frac{1 - r_2}{1 + r_2}\frac{1}{1 - r_2 z_1 z_2}. \tag{A13}$$

References

Ammon, C. J. (1991). The isolation of receiver effects from teleseismic P waveforms. *Bulletin of the Seismological Society of America*, *81*(6), 2504–2510.

Anandakrishnan, S., & Winberry, J. P. (2004). Antarctic subglacial sedimentary layer thickness from receiver function analysis. *Global and Planetary Change*, *42*(1–4), 167–176. https://doi.org/10.1016/j.gloplacha.2003.10.005

Becker, G., & Knapmeyer-Endrun, B. (2018). Crustal thickness across the Trans-European Suture Zone from ambient noise autocorrelations. *Geophysical Journal International*, *212*(2), 1237–1254. https://doi.org/10.1093/gji/ggx485

Bensen, G. D., Ritzwoller, M. H., Barmin, M. P., Levshin, A. L., Lin, F., Moschetti, M. P., et al. (2007). Processing seismic ambient noise data to obtain reliable broad-band surface wave dispersion measurements. *Geophysical Journal International*, *169*(3), 1239–1260. https://doi.org/10.1111/j.1365-246X.2007.03374.x

Bingham, R., & Siegert, M. (2007). Radio-echo sounding over polar ice masses. *Journal of Environmental and Engineering Geophysics*, *12*(1), 47–62. https://doi.org/10.2113/JEEG12.1.47

Chaput, J., Aster, R. C., Huerta, A., Sun, X., Lloyd, A., Wiens, D., et al. (2014). The crustal thickness of West Antarctica. *Journal of Geophysical Research: Solid Earth*, *119*, 378–395. https://doi.org/10.1002/2013JB010642

Claerbout, J. (1968). Synthesis of a layered medium from its acoustic transmission response. *Geophysics*, *33*(2), 264–269. https://doi.org/10.1190/1.1439927

Diez, A., Bromirski, P. D., Gerstoft, P., Stephen, R. A., Anthony, R. E., Aster, R. C., et al. (2016). Ice shelf structure derived from dispersion curve analysis of ambient seismic noise, Ross Ice Shelf, Antarctica. *Geophysical Journal International*, *205*(2), 785–795. https://doi.org/10.1093/gji/ggw036

Efron, B., & Tibshirani, R. (1991). Statistical data analysis in the computer age. *Science*, *253*(5018), 390–395. https://doi.org/10.1126/science.253.5018.390

Ekström, G., Nettles, M., & Dziewoński, A. M. (2012). The global CMT project 2004–2010: Centroid-moment tensors for 13,017 earthquakes. *Physics of the Earth and Planetary Interiors*, *200-201*, 1–209. https://doi.org/10.1016/j.pepi.2012.04.002

Frasier, C. W. (1970). Discrete time solution of plane p-sv waves in a plane layered medium. *Geophysics*, *35*(2), 197–219. https://doi.org/10.1190/1.1440085

Fretwell, P., Pritchard, H. D., Vaughan, D. G., Bamber, J. L., Barrand, N. E., Bell, R., et al. (2013). Bedmap2: Improved ice bed, surface and thickness datasets for Antarctica. *The Cryosphere*, *7*(1), 375–393. https://doi.org/10.5194/tc-7-375-2013

Gagnon, R. E., Kiefte, H., Clouter, M. J., & Whalley, E. (1988). Pressure dependence of the elastic constants of ice Ih to 2.8 kbar by Brillouin spectroscopy. *The Journal of Chemical Physics*, *89*(8), 4522–4528. https://doi.org/10.1063/1.454792

Gorbatov, A., Saygin, E., & Kennett, B. L. N. (2013). Crustal properties from seismic station autocorrelograms. *Geophysical Journal International*, *192*(2), 861–870. https://doi.org/10.1093/gji/ggs064

Hansen, S. E., Julià, J., Nyblade, A. A., Pyle, M. L., Wiens, D. A., & Anandakrishnan, S. (2009). Using S wave receiver functions to estimate crustal structure beneath ice sheets: An application to the Transantarctic Mountains and East Antarctic craton. *Geochemistry, Geophysics, Geosystems*, *10*, Q08014. https://doi.org/10.1029/2009GC002576

Hansen, S. E., Nyblade, A. A., Heeszel, D. S., Wiens, D. A., Shore, P., & Kanao, M. (2010). Crustal structure of the Gamburtsev Mountains, East Antarctica, from S-wave receiver functions and Rayleigh wave phase velocities. *Earth and Planetary Science Letters*, *300*(3–4), 395–401. https://doi.org/10.1016/j.epsl.2010.10.022

Kennett, B. L. N. (2015). Lithosphere–asthenosphere P-wave reflectivity across Australia. *Earth and Planetary Science Letters*, *431*, 225–235. https://doi.org/10.1016/j.epsl.2015.09.039

Kennett, B. L. N., Engdahl, E. R., & Buland, R. (1995). Constraints on seismic velocities in the Earth from traveltimes. *Geophysical Journal International*, *122*(1), 108–124. https://doi.org/10.1111/j.1365-246X.1995.tb03540.x

Kennett, B. L. N., Saygin, E., & Salmon, M. (2015). Stacking autocorrelograms to map Moho depth with high spatial resolution in southeastern Australia. *Geophysical Research Letters*, *42*, 7490–7497. https://doi.org/10.1002/2015GL065345

Kohnen, H. (1974). The temperature dependence of seismic waves in ice. *Journal of Glaciology*, *13*(67), 144–147. https://doi.org/10.1017/S0022143000023467

Langston, C. A. (1979). Structure under Mount Rainier, Washington, inferred from teleseismic body waves. *Journal of Geophysical Research*, *84*(B9), 4749–4762. https://doi.org/10.1029/JB084iB09p04749

Lawrence, J. F., Wiens, D. A., Nyblade, A. A., Anandakrishnan, S., Shore, P. J., & Voigt, D. (2006). Rayleigh wave phase velocity analysis of the Ross Sea, Transantarctic Mountains, and East Antarctica from a temporary seismograph array. *Journal of Geophysical Research*, *111*, B06302. https://doi.org/10.1029/2005JB003812

Lévêque, J.-J., Maggi, A., & Souriau, A. (2010). Seismological constraints on ice properties at Dome C, Antarctica, from horizontal to vertical spectral ratios. *Antarctic Science*, *22*(5), 572–579. https://doi.org/10.1017/S0954102010000325

Lloyd, A. J., Nyblade, A. A., Wiens, D. A., Hansen, S. E., Kanao, M., Shore, P. J., & Zhao, D. (2013). Upper mantle seismic structure beneath central East Antarctica from body wave tomography: Implications for the origin of the Gamburtsev Subglacial Mountains. *Geochemistry, Geophysics, Geosystems*, *14*, 902–920. https://doi.org/10.1002/ggge.20098

Lythe, M. B., Vaughan, D. G., & the BEDMAP Consortium (2001). BEDMAP: A new ice thickness and subglacial topographic model of Antarctica. *Journal of Geophysical Research*, *106*(B6), 11,335–11,351. https://doi.org/10.1029/2000JB900449

Nishitsuji, Y., Rowe, C. A., Wapenaar, K., & Draganov, D. (2016). Reflection imaging of the Moon's interior using deep-moonquake seismic interferometry. *Journal of Geophysical Research: Planets*, *121*, 695–713. https://doi.org/10.1002/2015JE004975

Oren, C., & Nowack, R. L. (2017). Seismic body-wave interferometry using noise autocorrelations for crustal structure. *Geophysical Journal International*, *208*(1), 321–332. https://doi.org/10.1093/gji/ggw394

Paulssen, H., Visser, J., & Nolet, G. (1993). The crustal structure from teleseismic P-wave coda—I. Method. *Geophysical Journal International*, *112*(1), 15–25. https://doi.org/10.1111/j.1365-246X.1993.tb01433.x

Phạm, T.-S., & Tkalčić, H. (2017). On the feasibility and use of teleseismic P wave coda autocorrelation for mapping shallow seismic discontinuities. *Journal of Geophysical Research: Solid Earth*, *122*, 3776–3791. https://doi.org/10.1002/2017JB013975

Plewes, L. A., & Hubbard, B. (2001). A review of the use of radio-echo sounding in glaciology. *Progress in Physical Geography*, *25*(2), 203–236. https://doi.org/10.1177/030913330102500203

Podolskiy, E. A., & Walter, F. (2016). Cryoseismology. *Reviews of Geophysics*, *54*, 708–758. https://doi.org/10.1002/2016RG000526

Ramirez, C., Nyblade, A., Hansen, S. E., Wiens, D. A., Anandakrishnan, S., Aster, R. C., et al. (2016). Crustal and upper-mantle structure beneath ice-covered regions in Antarctica from S-wave receiver functions and implications for heat flow. *Geophysical Journal International*, *204*(3), 1636–1648. https://doi.org/10.1093/gji/ggv542

Ruigrok, E., & Wapenaar, K. (2012). Global-phase seismic interferometry unveils P-wave reflectivity below the Himalayas and Tibet. *Geophysical Research Letters*, *39*, L11303. https://doi.org/10.1029/2012GL051672

Saygin, E., Cummins, P. R., & Lumley, D. (2017). Retrieval of the P wave reflectivity response from autocorrelation of seismic noise: Jakarta Basin, Indonesia. *Geophysical Research Letters*, *44*, 792–799. https://doi.org/10.1002/2016GL071363

Schenk, P. M. (2002). Thickness constraints on the icy shells of the Galilean satellites from a comparison of crater shapes. *Nature*, *417*(6887), 419–421. https://doi.org/10.1038/417419a

Schimmel, M., & Paulssen, H. (1997). Noise reduction and detection of weak, coherent signals through phase-weighted stacks. *Geophysical Journal International*, *130*(2), 497–505. https://doi.org/10.1111/j.1365-246X.1997.tb05664.x

Seht, M. I., & Wohlenberg, J. (1999). Microtremor measurements used to map thickness of soft sediments. *Bulletin of the Seismological Society of America*, *89*(1), 250–259.

Snieder, R., & Larose, E. (2013). Extracting Earth's elastic response from noise measurements. *The Annual Review of Earth and Planetary Sciences*, *41*(1), 183–206. https://doi.org/10.1146/annurev-earth-050212-123936

Stein, S., & Wysession, M. (2003). *An introduction to seismology, earthquakes, and earth structure*, (1st ed.). Malden, MA: Blackwell Publishing.

Sun, W., & Kennett, B. L. N. (2016). Receiver structure from teleseisms: Autocorrelation and cross correlation. *Geophysical Research Letters*, *43*, 6234–6242. https://doi.org/10.1002/2016GL069564

Tibuleac, I. M., & von Seggern, D. (2012). Crust-mantle boundary reflectors in Nevada from ambient seismic noise autocorrelations. *Geophysical Journal International*, *189*(1), 493–500. https://doi.org/10.1111/j.1365-246X.2011.05336.x

Wapenaar, K., Draganov, D., Snieder, R., Campman, X., & Verdel, A. (2010). Tutorial on seismic interferometry: Part 1—Basic principles and applications. *Geophysics*, *75*(5), 75A195–75A209. https://doi.org/10.1190/1.3457445

Wittlinger, G., & Farra, V. (2012). Observation of low shear wave velocity at the base of the polar ice sheets: Evidence for enhanced anisotropy. *Geophysical Journal International*, *190*(1), 391–405. https://doi.org/10.1111/j.1365-246X.2012.05474.x

Wittlinger, G., & Farra, V. (2015). Evidence of unfrozen liquids and seismic anisotropy at the base of the polar ice sheets. *Polar Science*, *9*(1), 66–79. https://doi.org/10.1016/j.polar.2014.07.006

Yan, P., Li, Z., Li, F., Yang, Y., Hao, W., & Bao, F. (2018). Antarctic ice sheet thickness estimation using the horizontal-to-vertical spectral ratio method with single-station seismic ambient noise. *The Cryosphere*, *12*(2), 795–810. https://doi.org/10.5194/tc-12-795-2018

Zhan, Z., Ni, S., Helmberger, D. V., & Clayton, R. W. (2010). Retrieval of Moho-reflected shear wave arrivals from ambient seismic noise. *Geophysical Journal International*, *182*(1), 408–420. https://doi.org/10.1111/j.1365-246X.2010.04625.x

Zhan, Z., Tsai, V. C., Jackson, J. M., & Helmberger, D. (2014). Ambient noise correlation on the Amery Ice Shelf, East Antarctica. *Geophysical Journal International*, *196*(3), 1796–1802. https://doi.org/10.1093/gji/ggt488